Progress In Electromagnetics Research, Vol. 119, 345–361, 2011

MODAL ANALYSIS OF METAL-STUB PHOTONIC BAND GAP STRUCTURES IN A PARALLEL-PLATE WAVEGUIDE

C. P. Yuan and T. H. Chang*

Department of Physics, National Tsing Hua University, 101 Section 2 Kuang Fu Road, Hsinchu, Taiwan

Abstract—This work presents a theoretical method to solve metal-stub photonic-band-gap (PBG) problems based on the multiple-scattering and modal analysis methods. The multiple-scattering method is generalized, which replaces the scattering coefficient by a mode-coupling matrix. Corresponding sizes between the full dielectric cylinder and the metal stub could be determined based on modal analysis. The metal stub can generate a similar frequency response to that of the full dielectric cylinder, implying that the metal stub is a good substitute for the dielectric cylinder. An experiment conducted at a low terahertz region verifies the theoretical predictions. This work offers a possibility to design two-dimensional photonic crystals using metal stub by adjusting its height for low terahertz applications.

1. INTRODUCTION

Previous studies have demonstrated that the metal parallel-plate waveguide (PPWG) is capable of propagating terahertz pulses [1–6]. With no group-velocity dispersion, the transverse electromagnetic (TEM) mode of PPWG is characterized by undistorted and low-loss wave propagation. The two-dimensional (2D) PBG [7] structure is also brought up many applications in terahertz range, most using full metal or dielectric cylinders/holes [8–12]. Using dielectric cylinders or holes must consider their dielectric properties and frequency response, while using full metal cylinders generally has an extremely low transmission [13, 14]. A previous work devised a metal-stub shape for a 2D-PBG structure [13], in which an air gap is maintained between

Received 6 May 2011, Accepted 28 July 2011, Scheduled 15 August 2011

* Corresponding author: Tsun-Hun Chang (thschang@phys.nthu.edu.tw).

the metal stubs and another waveguide plate. This feature offers an additional degree of freedom in the design of the PBG structure since the metal stub height can be adjusted; in addition, the aspect ratio is not necessarily so high, making it relatively easy to fabricate. Unfortunately, the metal stubs break the 2D symmetry, which is not easily analyzed by the plane-wave expansion method or other theoretical methods. It could be solved by finite-difference time-domain method [15–20] or finite element method [21, 22], but they may need much computing time. Therefore, a theoretical method is developed to calculate this problem.

The third dimension of the wave is bound by PPWG, which differs from 2D-PBG structures in the optical ranges bound by total reflection between two dielectric materials [23]. Therefore, only the E-polarized wave (TEM mode, not transverse-magnetic-like, TM-like, mode) can be propagated in PPWG under the cutoff frequencies of other high order modes; in addition, no fundamental H-polarized wave could exist in PPWG [24]. Although this is an advantage for a single mode operation for the E-polarized wave, the PPWG systems cannot apply directly to the published theory of H-polarized wave. Therefore, this work focuses on the E-polarized wave.

This work presents a theoretical analysis of metal-stub PBG structures based on multiple-scattering [25–27] and modal analysis methods [28–31]. A PBG structure in the low terahertz region (W-band, 75–110 GHz) [11] is also exemplified to verify the theoretical prediction accuracy. Both theoretical and experimental results correlate well with each other.

2. MULTIPLE-SCATTERING METHOD

By using the multiple-scattering method, the transmission in the frequency domain for a finite crystal is obtained to locate the band gap [25–27]. All definitions are described first, followed by a generalization of the method to solve metal-stub problems in the final paragraph of this section. The incident wave is a plane wave e^{ikx} with a finite range w (from $y = -w/2$ to $y = w/2$) located at $x = -l$ in Cartesian coordinates (x, y), where k represents the wave number and $i \equiv \sqrt{-1}$. The Kirchhoff integral formula [32] with the infinite-space Green function [33] leads to

$$E_I(\vec{x}) = \frac{k}{4} e^{-ikl} \int_{-w/2}^{w/2} dy' \left[H_0\left(kr'\right) + iH_1\left(kr'\right) \cos\theta' \right], \qquad (1)$$

where E_I represents the incident electric field whose direction is perpendicular to the plates, $r' \equiv \sqrt{(x+l)^2 + (y-y')^2}$, $\cos\theta' \equiv$

$(x+l)/r'$, (r,θ) denotes the polar coordinates, $\vec{x}$ denotes the observer's coordinates $(x,\ y)$, and H_0/H_1 denotes Hankel functions of the first kind of zero/first order. The incident wave can be rewritten as the sum of the Bessel functions of the first kind J_M for a particular cylinder j located at $\vec{x}_j = (r_j, \theta_j)$,

$$E_I(\vec{x}_{oj}) = \sum_{M=-\infty}^{\infty} \alpha_M(j) J_M(kr_{oj}) e^{iM\theta_{oj}}, \tag{2}$$

where $\vec{x}_{oj} = \vec{x} - \vec{x}_j = (r_{oj}, \theta_{oj})$, and $\alpha_M(j)$ represents the complex coefficient of the incident wave for cylinder j. By considering just one cylinder at the origin, the scattering wave is a linear combination of Hankel functions of the first kind $H_M(kr)e^{iM\theta}$ to match the radiation boundary condition. For the boundary condition at $r = a$ (where a denotes the radius of the cylinder), $e^{iM\theta}$ is orthogonal for different M, so the coefficient of $H_M(kr)e^{iM\theta}$ is determined simply by the coefficient of $J_M(kr)e^{iM\theta}$ of the incident wave. The ratio of those two coefficients is often defined as scattering coefficient A_M. In the multiple-scattering case, the scattering wave is

$$E_{Rj}(\vec{x}_{oj}) = \sum_{M=-\infty}^{\infty} \beta_M(j) H_M(kr_{oj}) e^{iM\theta_{oj}}, \tag{3}$$

where $\beta_M(j)$ represents the complex coefficient of the scattering wave for cylinder j. For cylinder $\tilde{i}$, the equivalent incident wave is $E_I(\vec{x}_{o\tilde{i}}) + \sum_{j\neq\tilde{i}} E_{Rj}(\vec{x}_{oj})$. Based on the addition theorem for cylindrical harmonics, $H_M(kr_{oj})e^{iM\theta_{oj}}$ can be expanded in terms of $J_M(kr_{o\tilde{i}})e^{iM\theta_{o\tilde{i}}}$, which gives

$$\beta_M(\tilde{i}) = A_M \left[\alpha_M(\tilde{i}) + \sum_{j\neq\tilde{i}} \sum_{N=-\infty}^{\infty} \beta_N(j) e^{i(N-M)(\theta_{j\tilde{i}}+\pi)} H_{N-M}(kr_{j\tilde{i}}) \right], \tag{4}$$

where $\vec{x}_{j\tilde{i}} = \vec{x}_j - \vec{x}_{\tilde{i}} = (r_{j\tilde{i}}, \theta_{j\tilde{i}})$. For all different $\tilde{i}$, they form a set of self-consistent linear equations. After the equations are derived, $\beta_M(\tilde{i})$ can be obtained, which is equivalent to solving the entire problem. The sum of M cannot be infinite due to the calculation capability. Actually, our calculation converges for the sum of M running from -2 to 2.

The transmission coefficient can be defined in the far field region $kr \gg 1$ and $\theta = 0$. Now the incident wave can be approximated to $H_0(kr)kw/2$ [25, 34], and the total field amplitude is $H_0(kr)kw/2 + H_0(kr)\sum_j \sum_{M=-\infty}^{\infty} (-i)^M \beta_M(j) \exp(-ikr_j \cos\theta_j)$.

Thus, the transmission coefficient is

$$T = 1 + \frac{2}{kw} \sum_{j} \sum_{M=-\infty}^{\infty} (-i)^M \beta_M(j) e^{-ikr_j \cos\theta_j}. \tag{5}$$

For a PBG, the transmission is low, regardless of the direction of incident wave.

For either the metal or dielectric cylinder case, the scattering coefficient A_M can be derived by matching the boundary condition at $r = a$, in which only one TEM mode is considered. However, for metal-stub structures that break the 2D symmetry, some higher TE (transverse electric) and TM modes are generated when a TEM mode wave contacts the discontinuous boundary of a stub, further complicating the problem. In that case, the scattering wave includes the different multi-modes in PPWG, so $\alpha_M(j)$ and $\beta_M(j)$ now denote vectors composed of the TEM, TE, and TM modes in Eq. (4). Also, the scattering coefficient A_M should transfer to a matrix in order to represent the coupling of different modes, called a mode-coupling matrix. The transmission coefficient should be reconsidered for the other high order modes in Eq. (5) if the propagating constant of the high order mode is real. The following modal analysis demonstrates how to derive the mode-coupling matrices of scattering coefficients.

3. MODAL ANALYSIS IN THE CYLINDRICALLY SYMMETRIC CASE — $M = 0$

The following analysis is performed for the mode-coupling matrix of scattering coefficient A_0 for metal stubs at the origin. The electric and magnetic fields in PPWG for TM modes for cylindrical symmetry are as follows [24]:

$$E_z = X_0(k_{tm}r)\cos(k_m z) \tag{6}$$

$$E_r = \frac{-k_m}{k_{tm}} X_0'(k_{tm}r)\sin(k_m z) \tag{7}$$

$$B_\theta = \frac{ik}{k_{tm}c} X_0'(k_{tm}r)\cos(k_m z) \tag{8}$$

where $E_\theta = B_r = B_z = 0$, X_0 denotes the Bessel function of any kind of order zero, z represents the coordinate of the height in PPWG, $k_m \equiv m\pi/h$, m is a positive integer, h denotes the air gap between the parallel plates, $k_{tm} \equiv \sqrt{k^2 - k_m^2}$, $k \equiv \omega/c$, and c represents the speed of light. TE modes are orthogonal to TM and TEM modes in cylindrically symmetric case, so the TE modes do not require

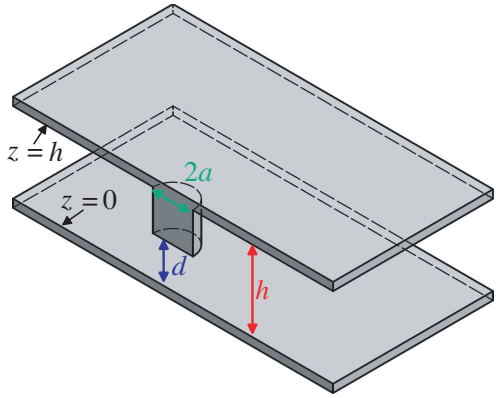

Figure 1. Schematic diagram of a metal stub in the PPWG.

consideration. The TEM mode can be treated as the lowest mode of the TM modes with $m = 0$.

The incident wave can be expanded as $E_z = \sum_{m=0}^{\infty} \delta_m J_0(k_{tm} r) \cos(k_m z)$ (other field components are similar). The reflected wave equation should satisfy the radiation boundary condition. This equation can be assumed as $E_z = \sum_{m=0}^{\infty} C_m H_0(k_{tm} r) \cos(k_m z)$. The transmitted wave equation can be $E_z = \sum_{n=0}^{\infty} D_n J_0(k'_{tn} r) \cos(k'_n z)$ because it should be well-defined at $r = 0$, where $k'_n \equiv n\pi/d$ and d represents the height of air gap from the lower plate to the bottom of the metal stub, as shown in Fig. 1.

At the boundary $r = a$, the equation of E_r is z-partial differential equation of B_θ multiply multiplied by $-ic/k$. Therefore, only the equations of E_z and B_θ should be considered as follows:

$$\sum_{m=0}^{\infty} \left[\delta_m J_0(k_{tm} a) + C_m H_0(k_{tm} a)\right] \cos(k_m z) = \begin{cases} \sum\limits_{n=0}^{\infty} D_n J_0(k'_{tn} a) \cos(k'_n z) & 0 \le z \le d \\ 0 & h \ge z > d \end{cases}, \tag{9}$$

$$\sum_{m=0}^{\infty} \left[\delta_m J'_0(k_{tm} a) + C_m H'_0(k_{tm} a)\right] \frac{1}{k_{tm}} \cos(k_m z) = \sum_{n=0}^{\infty} D_n \frac{1}{k'_{tn}} J'_0(k'_{tn} a) \cos(k'_n z) \quad 0 \le z \le d. \tag{10}$$

Multiplying Eq. (9) by $\cos(k_m z)$ followed by integration with z from 0 to h, and multiplying Eq. (10) by $\cos(k'_n z)$ followed by integration

with z from 0 to d reduce those equations in matrix representations as follows:

$$\begin{cases} C = M_2 D - \frac{J_0(k_{tm}a)}{H_0(k_{tm}a)}\delta \\ M_4 \left[C + \frac{J_0'(k_{tm}a)}{H_0'(k_{tm}a)}\delta\right] = J_0'(k_{tn}'a)D \end{cases}, \tag{11}$$

where M_2 and M_4 are defined as follows:

$$[M_2]_{mn} = \frac{J_0(k_{tn}'a)}{H_0(k_{tm}a)} \frac{\int_0^d \cos(k_n'z)\cos(k_m z)dz}{\int_0^h \cos^2(k_m z)dz}, \tag{12}$$

$$[M_4]_{nm} = \frac{k_{tn}' H_0'(k_{tm}a)}{k_{tm}} \frac{\int_0^d \cos(k_m z)\cos(k_n'z)dz}{\int_0^d \cos^2(k_n'z)dz}, \tag{13}$$

where $m = 0, 1, 2, 3, \ldots$; C, D, and δ are column vectors defined with $[C]_m = C_m$, $[D]_m = D_m$, and $[\delta]_m = \delta_m$; $J_0(k_{tm}a)/H_0(k_{tm}a)$, $J_0'(k_{tm}a)/H_0'(k_{tm}a)$, and $J_0'(k_{tn}'a)$ are diagonal matrices defined as $[J_0(k_{tm}a)/H_0(k_{tm}a)]_{m,m} = J_0(k_{tm}a)/H_0(k_{tm}a)$.

Solving the equations gives,

$$D = \left[M_4 M_2 - J_0'(k_{tn}'a)\right]^{-1} M_4 \left[\frac{J_0(k_{tm}a)}{H_0(k_{tm}a)} - \frac{J_0'(k_{tm}a)}{H_0'(k_{tm}a)}\right]\delta. \tag{14}$$

The mode-coupling matrix of the scattering coefficient is

$$\overleftrightarrow{A}_0 = M_2 \left[M_4 M_2 - J_0'(k_{tn}'a)\right]^{-1} M_4 \left[\frac{J_0(k_{tm}a)}{H_0(k_{tm}a)} - \frac{J_0'(k_{tm}a)}{H_0'(k_{tm}a)}\right] - \frac{J_0(k_{tm}a)}{H_0(k_{tm}a)}. \tag{15}$$

The matrix converges when the number of modes exceeds 10. For $M \neq 0$, Appendix provides details of the derivation.

4. CASE STUDY — DIELECTRIC CYLINDER AND METAL STUB

If the air gap of PPWG is such smaller that cutoff frequency of any high order mode is higher than the operating frequency, those modes cannot propagate and decay quickly in a small range when they are generated. In this case, the multiple scattering for the high order modes is negligible. The mode-coupling matrices of scattering coefficients can be reduced to a scalar form as the mode-coupling coefficient from TEM mode to TEM mode. The problem is thus the same as the full cylinder case when the scattering coefficients are determined. If the scattering coefficients of the metal stub are occasionally the same as

the dielectric cylinder, a similar PBG is obtained based on the plane-wave expansion method [35, 36] in the dielectric cylinder. After the mapping between the metal stub and the dielectric cylinder is obtained, a similar property of PBG is also obtained for the metal stub structure. However, owing to the difficulty in matching all scattering coefficients in a board frequency range, a small radius of cylinder is chosen in this work to allow the high order A_m to be significantly smaller than A_0 [34]. Thus, only one A_0 should be considered.

When selecting a dielectric cylinder with a radius of 0.15 mm and relative dielectric constant of $\varepsilon_r = 8.9$, there is a PBG in $95 \sim 99$ GHz for the lattice constant 1.5 mm, as shown in Fig. 2(a). The dielectric cylinder corresponds to a metal stub with a radius of 0.2 mm and height of 0.53 mm ($h = 1.27$ mm), the property of the scattering coefficients A_0, as shown in Fig. 2(b). Figs. 2(c) and 2(d) show the multiple-scattering calculation results for two incident wave directions. In Fig. 2(c), for the incident wave in the crystal's Γ-X direction, the stop band is around $79 \sim 99$ GHz for the dielectric cylinders correlating well with Fig. 2(a). However, the stop band changes to $79 \sim 103$ GHz for the metal stubs because the scattering coefficient A_1 of the metal stub is higher than that of the dielectric cylinder, especially for a frequency exceeding 95 GHz. In Fig. 2(d) for incident wave in Γ-M direction of the crystal, the dielectric cylinders and the metal stubs resemble each other in terms of multiple-scattering calculation results. This finding suggests that PBG is larger (about $92 \sim 103$ GHz) for the metal stubs, which agrees well with the eigenfrequencies based on HFSS (High Frequency Structure Simulator, ANSYS) in Fig. 2(a).

Figure 3 shows the simulation results of HFSS for the field patterns of the stop band and the pass band. The transmission is large at the pass band in Fig. 3(a), and there is some focus of the incident wave, which responds to the transmission peak at approximately 76 GHz in Fig. 2(c). The incident wave decays rather quickly when it contacts the crystal, resulting in nearly no transmission at the stop band in Fig. 3(b). Notably, the theory presented in Section 2 is unable to consider the reflection effect of the source/receiver horn, while HFSS can verify such an effect. The source/receiver horn is designed properly to reduce the reflections bases on the HFSS simulations. Thus, the experimental apparatus is constructed using this structure.

Figure 4(a) displays the experimental apparatus whose interior is the same as in Fig. 3. Details of the apparatus can be found in Ref. [34]. Connected to a W-band network analyzer, the transmission can be measured from 75 GHz to 110 GHz. The crystal consists of a 15×15 grid with a space of 1.5 mm, and it is cut off 4 corners and forms an octagon, as shown in Fig. 4(b). The octagon preserves the

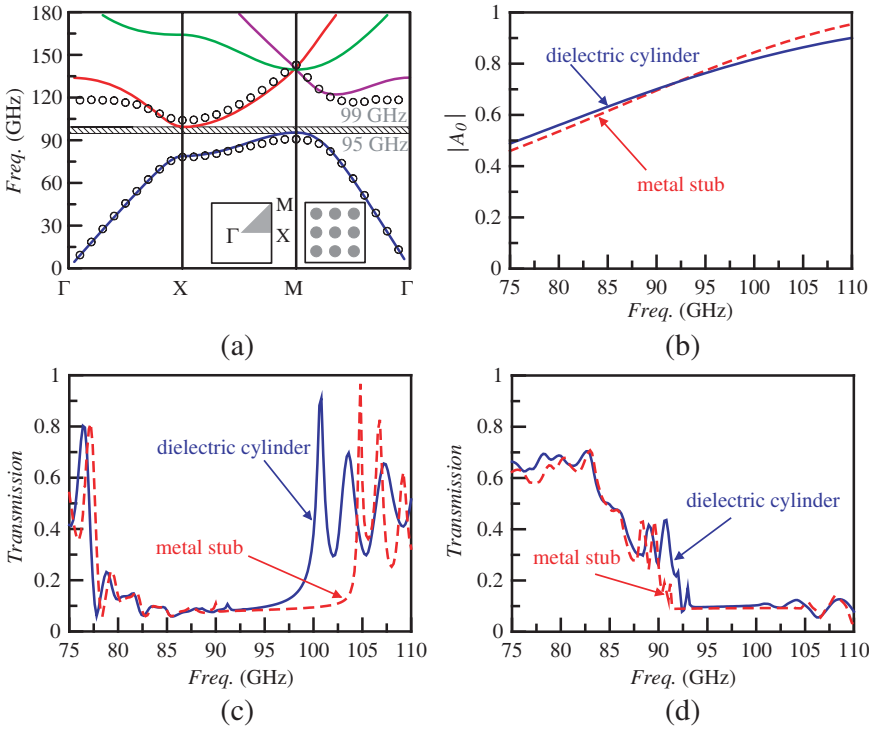

Figure 2. (a) Band structures of the crystals. The solid lines indicate the dispersion relation, and the hatched region indicates the band gap of 95 $\sim$ 99 GHz of dielectric cylinders with a relative dielectric constant of $\varepsilon_r = 8.9$, radius of 0.15 mm, and lattice constant of 1.5 mm. The black circles indicate the initial two eigenfrequencies of the metal stubs with a radius of 0.2 mm and height of 0.53 mm based on the eigenmode solution type of HFSS, and this band gap is 92 $\sim$ 103 GHz. (b) Absolute values of the scattering coefficient $|A_0|$ versus frequency. The solid and dash lines indicate the scattering coefficient of the dielectric cylinder [34] and the metal stub, respectively. Normalized transmission field amplitudes versus frequency for incident wave in (c) Γ-X and (d) Γ-M directions. The solid and dash lines indicate the field amplitudes of the dielectric cylinders and the metal stubs, respectively. The calculation settings are the same as the following experimental setting.

cross-section of the crystal for any direction of incident wave.

Figure 5 indicates that the experiment results that agree well with the calculation results by using the multiple-scattering method with $w = 20$ mm and $l = 30$ mm. The incident wave almost reflects to the

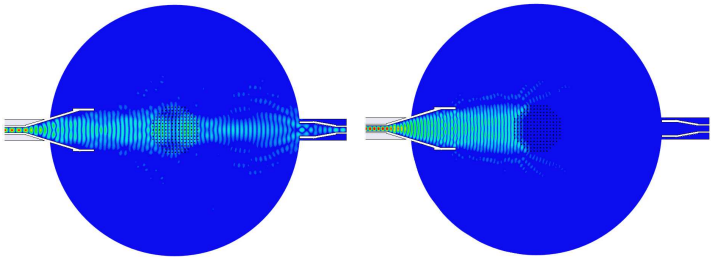

(a) (b)

Figure 3. Simulated diffraction patterns using HFSS at the frequencies of (a) 75 GHz (at pass band) and (b) 96 GHz (at stop band). The incident wave originates from the left-hand side, and the receiver is placed at the right-hand side. Γ-X direction of the crystal is parallel to the incident wave.

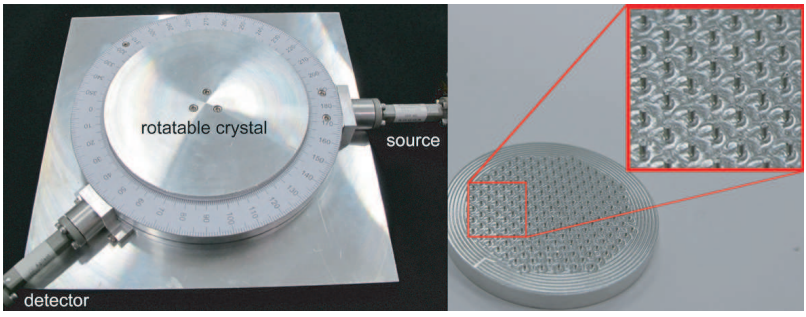

(a) (b)

Figure 4. Photographs of (a) experimental apparatus and (b) metal-stub PBG structure. Despite the numerous machining traces on the surface in the photo (b), its surface roughness is much smaller than the wavelength.

incident horn in the stop band such that the ripples are obvious, which are attributed to the connection gap of the horn in the apparatus. The machining error is larger than 0.01 mm, explaining why the height of metal stub is difficult to fabricate precisely; the experimental results thus converge slightly from the calculation results. Stub height (h-d) is critical to the overall performance, which could be proven in the modal analysis. Thus, accuracy of (h-d) for PBG applications using metal stubs should be of priority concern. In the transmission peak, although the some frequency shifts slightly, the calculation results and the experimental results closely correspond to each other.

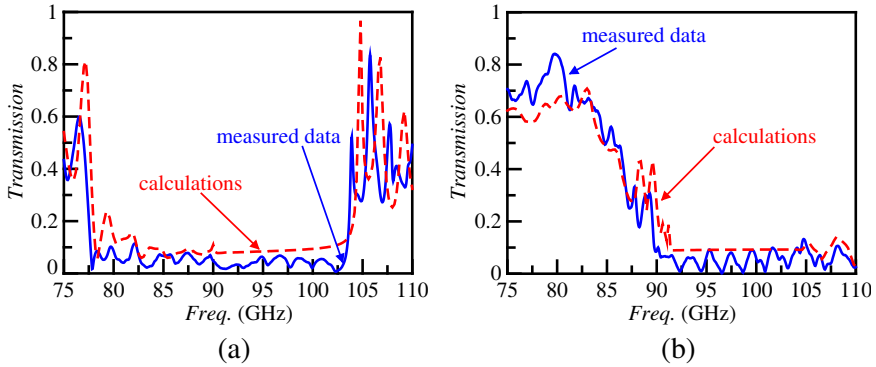

Figure 5. Normalized transmission field amplitudes versus frequency for incident wave in (a) Γ-X and (b) Γ-M directions. The solid and dash lines indicate the field amplitudes of the experimental results and the multiple scattering calculations, respectively.

5. CONCLUSIONS

This work described a generalized multiple-scattering method for metal-stub structures and modal analysis for scattering coefficients (matrices) of a metal stub in PPWG. The transmission (even full field patterns) can be calculated based on these theoretical methods. The proposed method can also analyze other 2D-PBG structures that break the 2D symmetry like holes.

A case study involving photonic band gap verifies that the dielectric-cylinder structure can be replaced with metal stubs in a PPWG. Additionally, the air gap can always be shortened to raise the high-order-mode cutoff frequency over the operating frequency range. When an adequate dielectric material cannot be obtained or is too difficult to fabricate, the metal-stub structures can be used to substitute the dielectric structures.

ACKNOWLEDGMENT

The authors would like to thank the National Science Council of the Republic of China, Taiwan (Contract No. NSC98-2112-M-007-003-MY3).

APPENDIX A.

The following analysis is performed for the mode-coupling matrix of the scattering coefficient A_M for metal stubs at the origin. The electric and magnetic fields in the PPWG for TM and TE modes are as follows [24]:

TM mode

$$\begin{aligned} E_z &= X_M(k_{tm}r)e^{iM\theta}\cos(k_m z) \\ E_r &= \frac{-k_m}{k_{tm}}X'_M(k_{tm}r)e^{iM\theta}\sin(k_m z) \\ E_\theta &= \frac{-ik_m M}{k_{tm}^2 r}X_M(k_{tm}r)e^{iM\theta}\sin(k_m z) \\ B_r &= \frac{kM}{k_{tm}^2 cr}X_M(k_{tm}r)e^{iM\theta}\cos(k_m z) \\ B_\theta &= \frac{ik}{k_{tm}c}X'_M(k_{tm}r)e^{iM\theta}\cos(k_m z) \\ B_z &= 0, \end{aligned} \tag{A1}$$

TE mode

$$\begin{aligned} E_z &= 0 \\ E_r &= \frac{-kM}{k_{tm}^2 r}X_M(k_{tm}r)e^{iM\theta}\sin(k_m z) \\ E_\theta &= \frac{-ik}{k_{tm}}X'_M(k_{tm}r)e^{iM\theta}\sin(k_m z) \\ B_r &= \frac{k_m}{k_{tm}c}X'_M(k_{tm}r)e^{iM\theta}\cos(k_m z) \\ B_\theta &= \frac{ik_m M}{k_{tm}^2 cr}X_M(k_{tm}r)e^{iM\theta}\cos(k_m z) \\ B_z &= \frac{1}{c}X_M(k_{tm}r)e^{iM\theta}\sin(k_m z), \end{aligned} \tag{A2}$$

where X_M denotes the Bessel function of any kind of order M, z denotes the coordinate of the height in PPWG, $k_m \equiv m\pi/h$, and $k_{tm} \equiv \sqrt{k^2 - k_m^2}$.

The incident TM wave can be expanded as $E_z = \sum_{m=0}^{\infty}\delta_m J_M(k_{tm}r)e^{iM\theta}\cos(k_m z)$; the incident TE wave can be expanded as $B_z = \sum_{m=1}^{\infty}\Delta_m 1/cJ_M(k_{tm}r)e^{iM\theta}\cos(k_m z)$. The reflected TM wave can be assumed as $E_z = \sum_{m=0}^{\infty}C_m H_M(k_{tm}r)e^{iM\theta}\cos(k_m z)$; the reflected TE wave can be assumed as $B_z = \sum_{m=1}^{\infty}P_m 1/cH_M(k_{tm}r)e^{iM\theta}\sin(k_m z)$. The transmitted TM wave equations can be amused as $E_z = \sum_{n=0}^{\infty}D_n J_M(k'_{tn}r)e^{iM\theta}\cos(k'_n z)$; the transmitted TE wave equations

can be assumed as $B_z = \sum_{n=1}^{\infty} Q_n J_M(k'_{tn} r) e^{iM\theta} \cos(k'_n z)$, where $k'_n \equiv n\pi/d$.

At the boundary $r = a$, the equation of E_r is the B_θ's z-partial differential equation multiplied by $-ic/k$ then plus the B_z's equation multiplied by $-cM/(kr)$; the equation of B_r is the E_θ's z-partial differential equation multiplied by $i/(ck)$ then plus the E_z's equation multiplying $M/(ckr)$. So only the equations of E_θ, E_z, B_z, and B_θ should be considered, which show as follows:

$$\sum_{m=1}^{\infty} \left\{ \frac{k_m M}{k_{tm}^2 a} \left[C_m H_M(k_{tm} a) + \delta_m J_M(k_{tm} a) \right] + \frac{k}{k_{tm}} \left[P_m H'_M(k_{tm} a) + \Delta_m J'_M(k_{tm} a) \right] \right\} \sin(k_m z)$$

$$= \begin{cases} \sum_{n=1}^{\infty} \left[\frac{k'_n M}{k'^2_{tn} a} D_n J_M(k'_{tn} a) + \frac{k}{k'_{tn}} Q_n J'_M(k'_{tn} a) \right] \sin(k'_n z) & z \le d \\ 0 & z > d \end{cases} \tag{A3}$$

$$\sum_{m=0}^{\infty} \left[C_m H_M(k_{tm} a) + \delta_m J_M(k_{tm} a) \right] \cos(k_m z)$$

$$= \begin{cases} \sum_{n=0}^{\infty} D_n J_M(k'_{tn} a) \cos(k'_n z) & z \le d \\ 0 & z > d \end{cases} \tag{A4}$$

$$\sum_{m=1}^{\infty} \left[P_m H_M(k_{tm} a) + \Delta_m J_M(k_{tm} a) \right] \sin(k_m z)$$

$$= \sum_{n=1}^{\infty} Q_n J_M(k'_{tn} a) \sin(k'_n z) \quad z \le d \tag{A5}$$

$$\sum_{n=0}^{\infty} \left\{ \frac{k}{k_{tm}} \left[C_m H'_M(k_{tm} a) + \delta_m J'_M(k_{tm} a) \right] + \frac{k_m M}{k_{tm}^2 a} \left[P_m H_M(k_{tm} a) + \Delta_m J_M(k_{tm} a) \right] \right\} \cos(k_m z)$$

$$= \sum_{n=0}^{\infty} \left[\frac{k}{k'_{tn}} D_n J'_M(k'_{tn} a) + \frac{k'_n M}{k'^2_{tn} a} Q_n J_M(k'_{tn} a) \right] \cos(k'_n z) \quad z \le d \tag{A6}$$

Multiplying Eq. (A3) by $\sin(k_m z)$ then integrated with z from 0 to h, multiplying Eq. (A4) by $\cos(k_m z)$ then integrated with z from 0 to h, multiplying Eq. (A5) by $\sin(k'_n z)$ then integrated with z from 0 to d, and multiplying Eq. (A6) by $\cos(k'_n z)$ then integrated with z

from 0 to d give four equations as follows:

$$\frac{k_m M}{k_{tm} ka}\left[\frac{H_M(k_{tm}a)}{H'_M(k_{tm}a)}C_m + \frac{J_M(k_{tm}a)}{H'_M(k_{tm}a)}\delta_m\right] + P_m + \frac{J'_M(k_{tm}a)}{H'_M(k_{tm}a)}\Delta_m$$
$$= \sum_{n=1}^{\infty} M_{1mn}\left[\frac{k'_n M}{k'_{tn} ka}J_M(k'_{tn}a)D_n + J'_M(k'_{tn}a)Q_n\right] \tag{A7}$$

$$C_m + \frac{J_M(k_{tm}a)}{H_M(k_{tm}a)}\delta_{m0} = \sum_{n=0}^{\infty} M_{2mn}D_n \tag{A8}$$

$$\sum_{m=0}^{\infty} M_{3nm}\left[P_m + \frac{J_M(k_{tm}a)}{H_M(k_{tm}a)}\Delta_m\right] = J_M(k'_{tn}a)Q_n \tag{A9}$$

$$\sum_{m=0}^{\infty} M_{4nm}\left[C_m + \frac{J'_M(k_{tm}a)}{H'_M(k_{tm}a)}\delta_{m0}\right.$$
$$\left.+\frac{H_M(k_{tm}a)}{H'_M(k_{tm}a)}\frac{k_m M}{k_{tm} ka}\left(P_m + \frac{J_M(k_{tm}a)}{H_M(k_{tm}a)}\Delta_m\right)\right]$$
$$= J'_M(k'_{tn}a)D_n + \frac{k'_n M}{k'_{tn} ka}J_M(k'_{tn}a)Q_n \tag{A10}$$

where

$$[M_1]_{mn} = \frac{k_{tm}}{k'_{tn}H'_M(k_{tm}a)}\frac{\int_0^d \sin(k'_n z)\sin(k_m z)dz}{\int_0^h \sin^2(k_m z)dz}, \tag{A11}$$

$$[M_2]_{mn} = \frac{J_M(k'_{tn}a)}{H_M(k_{tm}a)}\frac{\int_0^d \cos(k'_n z)\cos(k_m z)dz}{\int_0^h \cos^2(k_m z)dz}, \tag{A12}$$

$$[M_3]_{nm} = H_M(k_{tm}a)\frac{\int_0^d \sin(k_m z)\sin(k'_n z)dz}{\int_0^d \sin^2(k'_n z)dz}, \tag{A13}$$

$$[M_4]_{nm} = \frac{k'_{tn}H'_M(k_{tm}a)}{k_{tm}}\frac{\int_0^d \cos(k_m z)\cos(k'_n z)dz}{\int_0^d \cos^2(k'_n z)dz}. \tag{A14}$$

Note where $[M_1]_{0n} \equiv 0$, and $[M_3]_{0m} \equiv 0$ for the convenience of the subsequent calculation.

Now we use reduced symbols to express the equations, defined as follows: $M/(ka) \to a$, $H'_M(k_{tm}a) \to H'_m$, $H_M(k_{tm}a) \to H_m$, $J'_M(k_{tm}a) \to J'_m$, $J_M(k_{tm}a) \to J_m$, $J'_M(k'_{tn}a) \to J'_n$, and $J_M(k'_{tn}a) \to J_n$.

In the matrix representation defined as Section 3, they should be

written as

$$\begin{cases} \frac{k_m a}{k_{tm}}\left(\frac{H_m}{H'_m}C + \frac{J_m}{H'_m}\delta\right) + P + \frac{J'_m}{H'_m}\Delta = M_1\left(\frac{k'_n a}{k'_{tn}}J_n D + J'_n Q\right) \\ C + \frac{J_m}{H_m}\delta = M_2 D \\ M_3\left(P + \frac{J_m}{H_m}\Delta\right) = J_n Q \\ M_4\left(C + \frac{J'_m}{H'_m}\delta + \frac{k_m a}{k_{tm}}\frac{H_m}{H'_m}P + \frac{k_m a}{k_{tm}}\frac{J_m}{H'_m}\Delta\right) = J'_n D + \frac{k'_n a}{k'_{tn}}J_n Q \end{cases} \tag{A15}$$

The solution is

$$\begin{cases} C = \left(M_2 M_a - \frac{J_m}{H_m}\right)\delta + M_2 M_b \Delta \\ P = \left(M_x + M_1 J'_n M_y M_x\right) M_a \delta + M_c \Delta \end{cases} \tag{A16}$$

where

$$M_c \equiv M_x M_b + M_1 J'_n M_y \left[M_x M_b + \left(\frac{J_m}{H_m} - \frac{J'_m}{H'_m}\right)\right] - \frac{J'_m}{H'_m}, \tag{A17}$$

$$M_b \equiv M_z \left[M_4 \frac{k_m a}{k_{tm}}\frac{H_m}{H'_m} - \left(\frac{k'_n a}{k'_{tn}}J_n - M_4 \frac{k_m a}{k_{tm}}\frac{H_m}{H'_m}M_1 J'_n\right) M_y\right] \left(\frac{J_m}{H_m} - \frac{J'_m}{H'_m}\right), \tag{A18}$$

$$M_a \equiv -M_z M_4 \left(\frac{J_m}{H_m} - \frac{J'_m}{H'_m}\right), \tag{A19}$$

$$M_z \equiv \left[J'_n - M_4 M_2 - M_4 \frac{k_m a}{k_{tm}}\frac{H_m}{H'_m}M_x + \left(\frac{k'_n a}{k'_{tn}}J_n - M_4 \frac{k_m a}{k_{tm}}\frac{H_m}{H'_m}M_1 J'_n\right) M_y M_x\right]^{-1}, \tag{A20}$$

$$M_y \equiv \left(J_n - M_3 M_1 J'_n\right)^{-1} M_3, \tag{A21}$$

$$M_x \equiv M_1 \frac{k'_n a}{k'_{tn}}J_n - \frac{k_m a}{k_{tm}}\frac{H_m}{H'_m}M_2. \tag{A22}$$

The mode-coupling matrix of the scattering coefficient A_M is a rearrangement of Eq. (A16).

REFERENCES

1. Mendis, R. and D. Grischkowsky, "Undistorted guided-wave propagation of subpicosecond terahertz pulses," *Opt. Lett.*, Vol. 26, No. 11, 846–848, 2001.
2. Mendis, R. and D. Gischkowsky, "THz interconnect with low-loss and low-group velocity dispersion," *IEEE Microw. Wireless Compon. Lett.*, Vol. 11, No. 11, 444–446, 2001.

3. Coleman, S. and D. Grischkowsky, "Parallel plate THz transmitter," *Appl. Phys. Lett.*, Vol. 84, No. 5, 654–656, 2004.
4. Nagel, M., P. Haring Bolivar, and H. Kurz, "Modular parallel-plate THz components for cost-efficient biosensing systems," *Semicond. Sci. Technol.*, Vol. 20, S281–S285, 2005.
5. Mendis, R., "Nature of subpicosecond terahertz pulse propagation in practical dielectic-filled parallel-plate waveguides," *Opt. Lett.*, Vol. 31, No. 17, 2643–2645, 2006.
6. Cooke, D. G. and P. Und Jepsen, "Optical modulation of terahertz pulses in a parallel plate waveguide," *Opt. Express*, Vol. 16, No. 19, 15123–15129, 2008.
7. Guida, G., A. de Lustrac, and A. Priou, "An introduction to photonic band gap (PBG) materials," *Progress In Electromagnetics Research*, Vol. 41, 1–20, 2003.
8. Bingham, A. L. and D. R. Grischkowsky, "Terahertz 2-D photonic crystal waveguides," *IEEE Microw. Wireless Compon. Lett.*, Vol. 18, No. 7, 428–430, 2008.
9. Lin, C., C. Chen, G. J. Schneider, P. Yao, S. Shi, A. Sharkawy, and D. W. Prather, "Wavelength scale terahertz two-dimensional photonic crystal waveguides," *Opt. Express*, Vol. 12, No. 23, 5723–5728, 2004.
10. Zhao, Y. and D. Grischkowsky, "Terahertz demonstrations of effectively two-dimensional photonic bandgap structures," *Opt. Lett.*, Vol. 31, No. 10, 1534–1536, 2006.
11. Shchegolkov, D. Y., C. E. Heath, and E. I. Simakov, "Low loss metal diplexer and combiner based on a photonic band gap channel-drop filter at 109 GHz," *Progress In Electromagnetics Research*, Vol. 111, 197–212, 2011.
12. Butt, H., Q. Dai, T. D. Wilkinson, and G. A. J. Amaratunga, "Photonic crystals & metamaterial filters based on 2D arrays of silicon nanopillars," *Progress In Electromagnetics Research*, Vol. 113, 179–194, 2011.
13. Bingham, A., Y. Zhao, and D. Grischkowsky, "THz parallel plate photonic waveguides," *Appl. Phys. Lett.*, Vol. 87, 051101-1–051101-3, 2005.
14. Tarot, A.-C., S. Collardey, and K. Mahdjoubi, "Numerical studies of metallic PBG structures," *Progress In Electromagnetics Research*, Vol. 41, 133–157, 2003.
15. Swillam, M. A., R. H. Gohary, M. H. Bakr, and X. Li, "Efficient approach for sensitivity analysis of lossy and leaky structures using FDTD," *Progress In Electromagnetics Research*, Vol. 94, 197–212,

2009.

16. Zhang, Y.-Q. and D.-B. Ge, "A unified FDTD approach for electromagnetic analysis of dispersive objects," *Progress In Electromagnetics Research*, Vol. 96, 155–172, 2009.
17. Zheng, G., B.-Z. Wang, H. Li, X.-F. Liu, and S. Ding, "Analysis of finite periodic dielectric gratings by the finite-difference frequency-domain method with the sub-entire-domain basis functions and wavelets," *Progress In Electromagnetics Research*, Vol. 99, 453–463, 2009.
18. Li, J., L.-X. Guo, and H. Zeng, "FDTD method investigation on the polarimetric scattering from 2-D rough surface," *Progress In Electromagnetics Research*, Vol. 101, 173–188, 2010.
19. Kusiek, A. and J. Mazur, "Hybrid finite-difference/mode-matching method for analysis of scattering from arbitrary configuration of rotationally-symmetrical posts," *Progress In Electromagnetics Research*, Vol. 110, 23–42, 2010.
20. Izadi, M., M. Z. A. Ab Kadir, C. Gomes, and W. F. Wan Ahmad, "An analytical second-FDTD method for evaluation of electric and magnetic fields at intermediate distances from lightning channel," *Progress In Electromagnetics Research*, Vol. 110, 329–352, 2010.
21. Zhang, P. F., S. X. Gong, and S. F. Zhao, "Fast hybrid FEM/CRE — UTD method to compute the radiation pattern of antennas on large carriers," *Progress In Electromagnetics Research*, Vol. 89, 75–84, 2009.
22. Vaseghi, B., N. Takorabet, and F. Meibody-Tabar, "Transient finite element analysis of induction machines with stator winding turn fault," *Progress In Electromagnetics Research*, Vol. 95, 1–18, 2009.
23. Benisty, H., D. Labilloy, C. Weisbuch, C. J. M. Smith, T. F. Krauss, D. Cassagne, A. Béraud, and C. Jouanin, "Radiation losses of waveguide-based two-dimensional photonic crystals: Positive role of the substrate," *Appl. Phys. Lett.*, Vol. 76, No. 5, 532–534, 2000.
24. Marcuvitz, N., *Waveguide Handbook*, Chapter 2, McGraw-Hill, New York, 1951.
25. Li, L.-M. and Z.-Q. Zhang, "Multiple-scattering approach to finite-sized photonic band-gap materials," *Phys. Rev. B*, Vol. 58, No. 15, 9587–9590, 1998.
26. Martin, P. A., *Multiple Scattering: Interaction of Time-Harmonic Waves with N obstacles*, Cambridge University Press, Cambridge, 2006.

27. Botten, L. C., R. C. McPhedran, N. A. Nicorovici, A. A. Asatryan, C. M. de Sterke, P. A. Robinson, K. Busch, G. H. Smith, and T. N. Langtry, "Rayleigh multipole methods for photonic crystal calculations," *Progress In Electromagnetics Research*, Vol. 41, 21–60, 2003.
28. Gesell, G. A. and I. R. Ciric, "Recurrence modal analysis for multiple waveguide discontinuities and its application to circular structures," *IEEE Tran. Microw. Theory Tech.*, Vol. 41, No. 3, 484–490, 1993.
29. Yao, H.-Y. and T.-H. Chang, "Effect of high-order modes on tunneling characteristics," *Progress In Electromagnetics Research*, Vol. 101, 291–306, 2010.
30. Noor Amin, A. S., M. Mirhosseini, and M. Shahabadi, "Modal analysis of multilayer conical dielectric waveguides for azimuthal invariant modes," *Progress In Electromagnetics Research*, Vol. 105, 213–229, 2010.
31. Canto, J. R., C. R. Paiva, and A. M. Barbosa, "Modal analysis of bi-isotropic H-guides," *Progress In Electromagnetics Research*, Vol. 111, 1–24, 2011.
32. Jackson, J. D., *Classical Electrodynamics*, Chapter 10, John Wiley & Sons, New York, 1998.
33. Economou, E. N., *Green's Functions in Quantum Physics*, Chapter 1, Springer-Verlag, Berlin, 2006.
34. Yuan, C. P., S. Y. Lin, T. H. Chang, and B. Y. Shew, "Millimeter-wave Bragg diffraction of microfabricated crystal structures," *Am. J. Phys.*, Vol. 79, No. 6, 619–623, 2011.
35. Joannopoulos, J. D., R. D. Meade, and J. N. Winn, *Photonic Crystals: Molding the Flow of Light*, Princeton University Press, Princeton, 1995.
36. Lourtioz, J.-M., H. Benisty, V. Berger, J.-M. Gérard, D. Maystre, and A. Tchelnokov, *Photonic Crystals: Towards Nanoscale Photonic Devices*, Chapter 1, Springer-Verlag, Berlin, 2005.